Computer Methods in Applied Mechanics and Engineering 429 (2024) 117160

Contents lists available at ScienceDirect

Computer Methods in Applied Mechanics and Engineering

journal homepage: www.elsevier.com/locate/cma

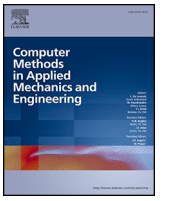

Dynamic crack propagation in elasto-plastic materials using phase-field virtual modelling method

Yiyang Liu [a], Yuan Feng [a,*], Zhangming Wu [b], Mehrisadat Makki Alamdari [a], Di Wu [c], Zhen Luo [d], Xiaojun Chen [a], Wei Gao [a,*]

[a] Centre for Infrastructure Engineering and Safety (CIES), School of Civil and Environmental Engineering, The University of New South Wales, Sydney, NSW 2052, Australia
[b] School of Engineering, Cardiff University, Cardiff, Wales CF24 3AA, UK
[c] Centre for Built Infrastructure Research (CBIR), School of Civil and Environmental Engineering, University of Technology Sydney, Sydney, NSW 2007, Australia
[d] School of Mechanical and Mechatronic Engineering, University of Technology Sydney, Sydney, NSW 2007, Australia

HIGHLIGHTS

- Phase-field virtual modelling method (PFVM) is proposed for dynamic fracture in elasto-plastic materials.
- Full-field uncertainties of PFVM enable reliable tracking of non-deterministic cracks.
- The exceptional capability of PFVM in complex 3D conditions is demonstrated.
- PFVM is validated in practical cases with both precision and efficiency.

ARTICLE INFO

Keywords:
Dynamic elasto-plastic fracture
Phase field method
Virtual modelling
Crack propagation prediction

ABSTRACT

In modern engineering, dynamic fracture failure because of unexpected load or human faults may lead to catastrophic disasters. Preventive structure design and real-time maintain suggestions based on accurate numerical simulation are critical, especially when plasticity develops. It remains a challenge to efficiently model dynamic crack propagation in elasto-plastic materials while the uncertain factors in service life may significantly increase the difficulty. In this paper, a phase-field virtual modelling method (PFVM), based on the features of the novel extended support vector regression (X-SVR) method, is proposed to tackle this non-deterministic problem. The phase field method is adopted for its outstanding performance in complex fracture problems, which provides solid reference data for the virtual model's training and verification. The PFM application to dynamic elasto-plastic fracture problems is validated in two practical engineering examples. The integrated virtual modelling technique is then proven capable of instantly providing precise crack propagation prediction under multiple complex uncertainties, making up-to-date numerical dynamic fracture simulation achievable and affordable. The proposed PFVM method can minimize the contradiction between accurate modelling and high computational cost and can be utilized in various extensions like sensitivity analysis or design optimization.

* Corresponding authors.
E-mail addresses: yuan.feng1@unsw.edu.au (Y. Feng), w.gao@unsw.edu.au (W. Gao).

https://doi.org/10.1016/j.cma.2024.117160
Received 7 April 2024; Received in revised form 19 May 2024; Accepted 12 June 2024
Available online 1 July 2024

1. Introduction

The elasto-plastic fracture behaviour under dynamic loading is one of the most important topics in modern engineering disciplines such as aerospace [1], medical treatment [2], and civil infrastructure [3–6]. The potential for catastrophic fracture failures, which pose considerable danger and risk to life as illustrated in Fig. 1, emphasizes the criticality of this area of research. In the service life of structural components, non-deterministic load conditions [7–10] is recognized as a significant contributor to global failure and should be considered in design to guarantee the safety and reliability of projects. Until now, it remains insufficient in the development of suitable numerical methods for simulating the dynamic fracture process while the balance between accuracy and computational cost is unsolved [11]. Furthermore, the incorporation of uncertainties into numerical simulations is challenging due to the required massive data. Consequently, the establishment of an effective computational framework to solve non-deterministic dynamic fracture problems in elasto-plastic materials is essential and impactful.

In the purpose of efficiently simulating dynamic crack propagation in elasto-plastic materials, the challenges can be categorized into three parts. The first one is the theoretical difficulties in dynamic fracture. Although researchers developed various mathematical theories and physics concepts [14–17] to closely describe the dynamic fracture since the early 20th century, it's not sufficient to fully explain the fracture mechanics in advanced materials and engineering science [18–20]. The dynamic load varies over time and causes unpredictable crack initiation or instable crack propagation. This will increase the computational complexity in finite element method [21]. Furthermore, the consideration of plasticity in elasto-plastic materials introduces another challenge because extra treatments should be implemented to describe the nonlinearity [22–25].

The second challenge is the choice of suitable simulation methods. Traditionally, the simulation of dynamic loads requires specific equipment like shaking tables, gas guns or high-speed cameras in the laboratory. The experiment settings are extremely complex, which may introduce human errors in the process. Numerous repeated experiments are preferred but hard to achieve for most elasto-plastic materials. Thus, numerical simulation methods provide a more economical way for the simulation compared to the high costs in experiments. Researchers have devoted a long research history to study fracture behaviours and understanding the relevant mechanics and principles. Several methods came to the forefront including the X-FEM [26] and crack band approach [27]. These methods are widely adopted but the performances of those vary a lot. Some may work very well for most 2D cases, but they are unacceptable in complex 3D problems. More recently, the phase field method (PFM) has gained considerable interest for its effectiveness in tracking complex crack patterns. The foundation of PFM can be traced back to the pioneering work of Francfort [28], Bourdin [29,30], and Miehe [31]. This approach then became popular in solving brittle fracture problems [32–39], and then extended to ductile fracture problems [22,40–44]. Important contributions include Ambati's model for elasto-plastic materials [45], Borden's study [46] on ductile fractures under significant strains, and comprehensive reviews by Alessi [47], Fang [23], and Molnár [48]. The emergence of PFM for ductile fracture provides reliable solution because of the following advantages. The PFM is based on energy functions and thus is naturally capable of handling complex crack topologies including crack branching or multiple 3D crack paths without applying special treatment or remeshing techniques. In addition, the PFM effectively couples damage and plasticity when the plastic deformation and strains lead to the potential of crack initiation and propagation. Another advantage by PFM is that the complex boundary conditions and load scenarios can be regularized simply, which is useful in solving dynamic problems.

The third challenge is the uncertainty analysis of non-deterministic cases. Non-deterministic factors are inevitable in contemporary engineering, such as inconstant loads (wind, vehicles, or impacts) and tiny defects in material. The acceptable nominal variation in the manufacturing process is typically limited to 1 % – 5 % but these seemingly negligible deviations may cause serious consequences in dynamic elasto-plastic fracture. Due to the development of plasticity, potential cracks accumulate along the load history. The underestimation of these minor imperfections or the over-simplicity of plasticity behaviour could lead to inaccurate crack propagation results and then to the global fracture failure [49]. Therefore, an uncertainty analysis should be conducted. The uncertainty analysis is a statistical process based on a large number of experimental or numerical simulations, rather than simply taking the maximum or minimum values. Engineers can improve the weak parts of the structure and optimize the structural design according to the analysis results [50,51]. Recently, one rising research direction is the use of machine learning techniques [52], like the extended support vector

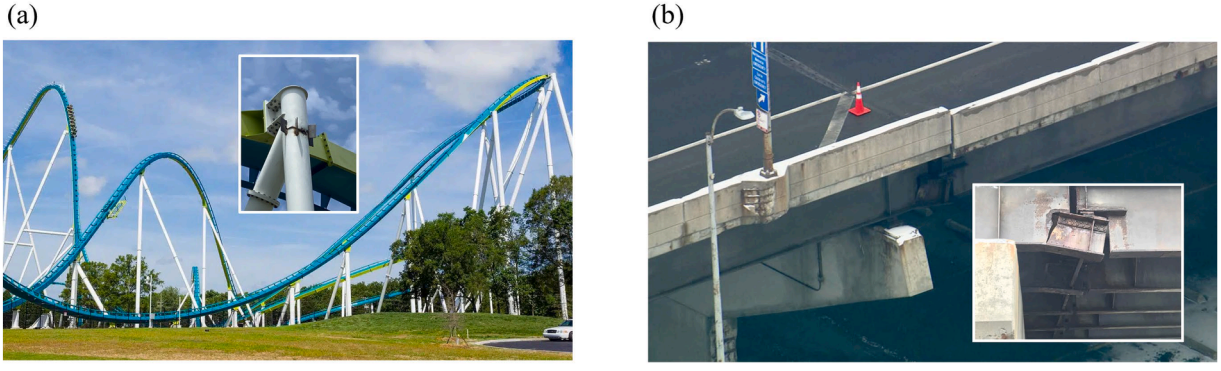

Fig. 1. (a) Cracked roller coaster column [12]. (b) Cracked beam on Lake Shore Drive Bridge [13].

regression (X-SVR) method [53]. These techniques may utilize sampling methods to extract information from the raw database and relieve the requirement of enormous statistical data. In other words, machine learning techniques are capable of learning from training datasets and predicting outcomes, and then pave the way for virtual models. As it literally meant, virtual models function as digital twins of physical models to acquire the prediction of dynamic elasto-plastic fracture responses without traditional FE calculations. Thus, virtual modelling can provide statistical information of fracture responses and is an efficient approach for uncertainty analysis of dynamic crack propagation in elasto-plastic materials.

Based on the methods discussed above, a novel phase-field virtual modelling method (PFVM) is proposed in the present study. PFVM provides an efficient means to deal with 3D dynamic elasto-plastic fracture problems under stochastic conditions, to comprehensively provide statistical information of fracture responses and to accurately predict future crack propagation paths with possibilities. Theoretically, PFVM is established on a base of numerous phase field simulations of dynamic elasto-plastic fracture problems, forming a global training dataset. In this process, the phase field method ensures the dependability of these numerical outcomes, and the training process incorporates a sampling technique first. This sampling technique involves the stochastic selection of system inputs with the associated fracture responses to facilitate a solid statistical representation of the whole database. Subsequently, the virtual model undergoes training using the dataset derived from this sampling process. In addition, another vital feature of PFVM is the application of the kernel-based X-SVR algorithm. X-SVR algorithm is orientated to handle the complexities of a high-dimensional, nonlinear elasto-plastic problem, thereby establishing a virtual governing relationship. With the trained virtual model, the PFVM framework demonstrates a remarkable proficiency in predicting dynamic elasto-plastic fracture responses with both efficiency and accuracy, then providing reliable statistical information for structural safety.

The paper is organized as follows. Chapter 2 provides a detailed explanation of deterministic dynamic elasto-plastic fracture analysis incorporating the phase field method. Chapter 3 extends the fracture analysis into non-deterministic cases with the considered uncertainties and numerical implementation. The procedure flowchart is also demonstrated in this chapter. In Chapter 4, two numerical examples and the verification results are discussed in detail.

2. Deterministic dynamic fracture analysis of elasto-plastic materials

The plasticity in the numerical simulation of dynamic fracture should be well considered due to its widespread existence. Considering the complex geometry and arbitrary crack propagation pattern, the phase field method is adopted in present study. The essential theories and formulations for dynamic fracture analysis in elasto-plastic materials are explained in this chapter. The detailed formulations about phase field method can be found in previous publications [36,48,54].

2.1. Theory of phase field method

In the theory of phase field method, the crack is represented as a surrounding cracked area instead of a discontinuity in the material. Under this assumption, two scalar values, the length parameter l_0 and the phase field value ϕ, are introduced to regularize the crack diffusion.

Considering an arbitrary solid $\Omega \subset \mathbb{R}^n (n = 2, 3)$ made of elasto-plastic material, the in-body crack boundary is denoted as Γ while the external applied boundary condition is marked as $\partial\Omega$. In the location $\boldsymbol{x}$, the displacement field at time t is $\boldsymbol{u}(\boldsymbol{x}, t) \subset \mathbb{R}^n$ while the phase field can be defined as $\phi(\boldsymbol{x})$. Assuming the solid body is under external loads including body force b^f and traction force T. Fig. 2 provides a 2D demonstration of these settings. In the meanwhile, the size of the affected area is formalised by l_0. The greater l_0 is, the wider the cracked material is. The mentioned scalar variable $\phi \in [0, 1]$ is adopted to represent the status of the solid by defining that the

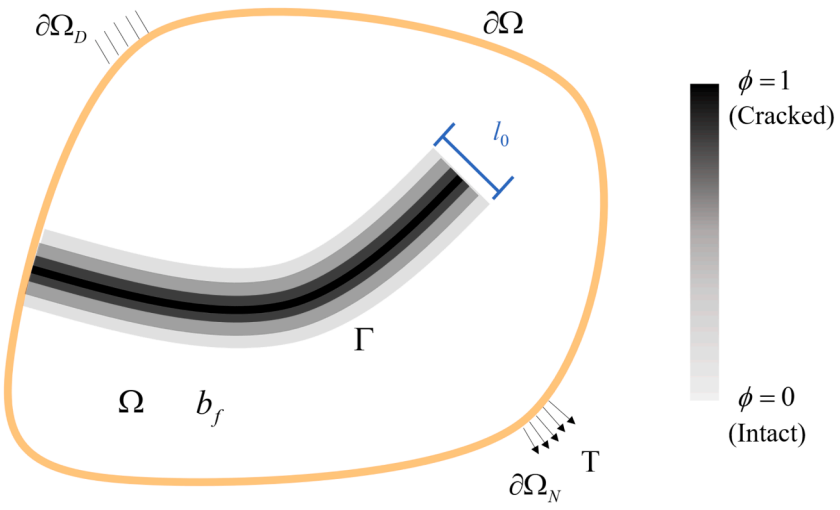

Fig. 2. Diffused crack model in phase field method.

material is broken when $\phi = 1$. The solid body remains intact if $\phi = 0$ respectively.

Francfort [28] proposed a variational method with the traditional Griffith's damage theory [55], in which the minimum energy to generate a new damage surface per unit area is defined as the critical fracture energy release rate G_c. Then, the energy function can be extracted within this energy-based theory. The total potential energy $\Psi_{pot}(\boldsymbol{u}, \Gamma)$ can be calculated as the sum of the elastic energy Ψ_e, plastic energy Ψ_p, fracture energy Ψ_{frac} and external forced energy Ψ_{ext}:

$$\Psi_{pot}(\boldsymbol{u}, \Gamma) = \Psi_e + \Psi_p + \Psi_{frac} - \Psi_{ext} \tag{1}$$

The first part of total potential energy is the elastic energy Ψ_e which can be decomposed into tensile and compressive components. In this implementation, only the tensile component can be cracked, and the cracked material is degraded by a degradation function [37,56].

The degradation function $g(\phi)$ is defined by:

$$g(\phi) = (1 - \phi)^2 + k \tag{2}$$

where k is a small number (10^{-8}) introduced for numerical stability when ϕ approaches 1.

The linear strain tensor $\boldsymbol{\varepsilon} = \boldsymbol{\varepsilon}(\boldsymbol{u})$ is formulated as:

$$\boldsymbol{\varepsilon}_{ij} = \frac{1}{2}\left(\frac{\partial \boldsymbol{u}_i}{\partial x_j} + \frac{\partial \boldsymbol{u}_j}{\partial x_i}\right) \tag{3}$$

Under the assumption of isotropic linear elasticity, the linear energy density $\psi_e(\varepsilon)$ is expressed in terms of Lamé constants λ and μas [31]:

$$\psi_e = \frac{1}{2}\lambda \boldsymbol{\varepsilon}_{ii}\boldsymbol{\varepsilon}_{jj} + \mu \boldsymbol{\varepsilon}_{ij}\boldsymbol{\varepsilon}_{ij} \tag{4}$$

Then, a degradation function containing the phase field value reduces the tensile strain energy density. Since the strain energy is composed of tensile strain (+) and compressive strain (-), the elastic energy is expressed as:

$$\Psi_e(\varepsilon) = \int_\Omega \psi_e d\Omega = \int_\Omega \left[(1 - \phi)^2 + k\right] \cdot \psi_e(\boldsymbol{\varepsilon})^+ + \psi_e(\boldsymbol{\varepsilon})^- d\Omega \tag{5}$$

In this implementation, the Von Mises yield criterion is adopted for its popularity universality. The plastic energy density ψ_p for a linear isotropic hardening is formulated as:

$$\psi_p(\boldsymbol{\delta}, d) = \frac{1}{2}\widetilde{H}(d)\boldsymbol{\delta}^2 \tag{6}$$

where $\widetilde{H}(d)$ is the hardening modulus of the degraded material and $\boldsymbol{\delta}$ is the accumulated plastic strain. The equivalent yield stress is denoted as $\widetilde{\sigma}_y$. It should be noted that both compression and tensile plastic strain contribute crack propagation equally, which is different from the condition of elastic strain. The plastic strain energy can be expressed as:

$$\Psi_p(\boldsymbol{\delta}) = \int_\Omega \left[(1 - \phi)^2 + k\right]\left(\frac{1}{2}\widetilde{H}(\phi)\boldsymbol{\delta}^2 + \widetilde{\sigma}_y\delta\right) d\Omega \tag{7}$$

As shown in Fig. 2, the crack surface is diffused by the length parameter l_0. According to the Griffith's theory, Miehe [57] developed the formulation describing the surface energy density function in the phase field theory as,

$$\gamma(\phi, \nabla\phi) = \frac{1}{2l_0} \cdot \phi^2 + \frac{l_0}{2} \cdot |\nabla\phi|^2 \tag{8}$$

With the crack surface density function (8), the considered fracture energy can be treated as a minimum energy to create a new crack area and then be written with critical energy release rate G_c as:

$$\int_\Gamma G_c d\Gamma \approx \int_\Omega G_c \cdot \gamma(l_0, \phi, \nabla\phi) d\Omega = \int_\Omega G_c \cdot \left[\frac{1}{2l_0} \cdot \phi^2 + \frac{l_0}{2} \cdot |\nabla\phi|^2\right] d\Omega \tag{9}$$

Combining the formula above, the total potential energy is expressed as:

$$\begin{aligned} \Psi_{pot}(u, \Gamma) &= \int_\Omega \psi_e(\varepsilon) d\Omega + \int_\Omega \psi_p(\delta) d\Omega + \int_\Gamma G_c(x) d\Gamma - \int_{\partial\Omega_N} T \cdot u d\partial\Omega_N \\ &= \int_\Omega \left[(1 - \phi)^2 + k\right] \cdot \psi_e(\varepsilon)^+ + \psi_e(\varepsilon)^- d\Omega + \int_\Omega \left[(1 - \phi)^2 + k\right]\left(\frac{1}{2}\widetilde{H}(\phi)\delta^2 + \widetilde{\sigma}_y\delta\right) d\Omega \\ &\quad + \int_\Omega G_c \cdot \frac{1}{2l_0} \cdot \phi^2 + G_c\frac{l_0}{2} \cdot |\nabla\phi|^2 d\Omega - \int_{\partial\Omega_N} \mathrm{T} \cdot u d\partial\Omega_N + \int_\Omega \mathrm{b}^f \cdot u d\Omega \end{aligned} \tag{10}$$

2.2. Staggered algorithm with quasi-Newton method

In this implementation, the staggered algorithm is adopted for the crack propagation analysis due to its numerical stability and robustness in dynamic fracture problems. In the staggered algorithm, which was firstly developed by Miehe et al. [57], the history field is added into the computation process to decouple the displacement field and the phase field. Under this setting, the history field H acts as the transfer station between these two independent fields.

The energy functional of dynamic fracture involves the Lagrange function is:

$$\mathrm{H}^{u} = D(\dot{\boldsymbol{u}}) - \Psi_{pot} \tag{11}$$

where $\dot{\boldsymbol{u}}$ contains the velocity vector. $D(\dot{\boldsymbol{u}})$ is the kinetic energy and can be expressed in terms of material density ρ:

$$D(\dot{\boldsymbol{u}}) = \frac{1}{2}\int_{\Omega} \dot{\boldsymbol{u}}^{T}\dot{\boldsymbol{u}}\rho d\Omega \tag{12}$$

Then, the phase field function can be derived as:

$$\mathrm{H}^{\phi} = \int_{\Omega} [G_c\gamma(\phi, \nabla\phi) + \phi \cdot \mathrm{H}]d\Omega \tag{13}$$

where the history field replaces the total potential energy term. In order to prevent the healing of the crack, the irreversibility of phase field value is restricted by Eq. (14),

$$\mathrm{H} = \begin{cases} \psi_e(\boldsymbol{\varepsilon})^{+} + \psi_p(\delta) - \psi_{frac}, & \psi_e(\boldsymbol{\varepsilon})^{+} + \psi_p(\delta) - \psi_{frac} > \mathrm{H}_n \\ \mathrm{H}_n, & \psi_e(\boldsymbol{\varepsilon})^{+} + \psi_p(\delta) - \psi_{frac} \le \mathrm{H}_n \end{cases} \tag{14}$$

where H_n is the previous step history field. Furthermore, Eq. (14) make the history field satisfies the Karush–Kuhn–Tucker (KKT) condition.

3. Non-deterministic dynamic fracture analysis in elasto-plastic materials

This section introduces the non-deterministic numerical implementation of the dynamic phase field model for elasto-plastic materials. The numerical application of ABAQUS using user subroutine (UEL) codes is thoroughly explained. Additionally, the non-deterministic parameters are defined in detail for enhanced comprehension. The implementation of virtual modelling techniques is subsequently demonstrated through a comprehensive flowchart.

3.1. Numerical implementation of non-deterministic dynamic elasto-plastic fracture

The staggered time-integration algorithm is adopted to solve the non-deterministic dynamic fracture problem in this paper. The Abaqus user subroutine is used to solve the displacement field and phase field iteratively.

The non-deterministic parameters are listed in Table 1. The first category of uncertainties involves material properties including Young's modulus, Poisson ratio, critical energy release rate, density, and initial yield stress. These parameters are commonly used to describe the mechanical properties of the material and it's essential to provide a statistical analysis of their influence on the fracture responses. In this study, the material property uncertainties are listed in a vector $\boldsymbol{\eta}^{M} = \left[E, \upsilon, G_c, \rho, \sigma_{y0}\right]^{T}$ [58,59]. Furthermore, the non-deterministic external loads are also considered and expressed in form of a vector $\boldsymbol{\eta}^{L} = \left[L_x, L_y, L_z\right]^{T}$. The footnote $\boldsymbol{\eta}_j$ represents the jth non-deterministic parameter set, and the vector $\boldsymbol{\eta}^{R}$ belongs to the probability space (Y, Λ, P) where Y denotes the sample space, P denotes the probability measure and Λ denotes the σ-algebra.

Table 1
Considered variabilities.

Category	Variational parameters	Abbreviations	Unit
Material properties	Young's modulus	$E\left(\boldsymbol{\eta}_j^{M}\right)$	GPa
	Poisson ratio	$\upsilon\left(\boldsymbol{\eta}_j^{M}\right)$	/
	Critical energy release rate	$G_c\left(\boldsymbol{\eta}_j^{M}\right)$	MPa•mm
	Density	$\rho\left(\boldsymbol{\eta}_j^{M}\right)$	kg/m^3
	Yield stress	$\sigma_{y0}\left(\boldsymbol{\eta}_j^{M}\right)$	MPa
Load conditions	x-direction displacement	$L_x\left(\boldsymbol{\eta}_j^{L}\right)$	mm
	y-direction displacement	$L_y\left(\boldsymbol{\eta}_j^{L}\right)$	mm
	z-direction displacement	$L_z\left(\boldsymbol{\eta}_j^{L}\right)$	mm

3D element type C3D4 in ABAQUS is implemented, so the shape function can be defined as $N = [N_1 \cdots N_4]$ and its corresponding spatial derivatives are given as:

$$B = \begin{bmatrix} \frac{\partial N_1}{\partial x} & \cdots & \frac{\partial N_4}{\partial x} \\ \frac{\partial N_1}{\partial y} & \cdots & \frac{\partial N_4}{\partial y} \\ \frac{\partial N_1}{\partial z} & \cdots & \frac{\partial N_4}{\partial z} \end{bmatrix} \tag{15}$$

The strain tensors and phase field value derivative can be given by:

$$\begin{aligned} \boldsymbol{\varepsilon} &= B^u \boldsymbol{u}(\eta^L) \\ \nabla\phi &= B^d \phi(\eta^M) \end{aligned} \tag{16}$$

For the dynamic cases, ABAQUS adopts the Hilber-Hughes-Taylor (HHT) method to achieve equilibrium and the equilibrium problem is listed as:

$$\begin{bmatrix} S_n^u\left(\boldsymbol{\eta}_j^R\right) & 0 \\ 0 & (1+\alpha)K_n^\phi(\boldsymbol{\eta}_j) \end{bmatrix} \begin{bmatrix} u_{n+\Delta t}(\boldsymbol{\eta}_j) \\ \phi_{n+\Delta t}(\boldsymbol{\eta}_j) \end{bmatrix} = -\begin{bmatrix} r_n^u(\boldsymbol{\eta}_j) \\ \alpha \boldsymbol{r}_{n-1}^d(\boldsymbol{\eta}_j) - (1+\alpha) r_n^\phi(\boldsymbol{\eta}_j) \end{bmatrix} \tag{17}$$

where $S_n^u(\boldsymbol{\eta}_j)$ and $K_n^\phi(\boldsymbol{\eta}_j)$ are the elementary stiffness in displacement field and phase field respectively. $r_n^u(\boldsymbol{\eta}_j)$ and $r_n^\phi(\boldsymbol{\eta}_j)$ are the residues. Parameter $\alpha = -0.05$ is the damping coefficient.

The tangent matrix $S_n^u(\boldsymbol{\eta}_j)$ of the displacement field is the sum of material and density matrix:

$$S_n^u(\boldsymbol{\eta}_j) = \mathbf{M}(\boldsymbol{\eta}_j)\frac{d\ddot{\boldsymbol{u}}}{d\boldsymbol{u}} + (1+\alpha)K_n^u(\boldsymbol{\eta}_j) \tag{18}$$

where the mass matrix can be obtained by,

$$\mathbf{M}(\boldsymbol{\eta}_j) = M_{kk} = \int_\Omega \left(N_{kj}^u\right)^T \rho(\boldsymbol{\eta}_j) N_{kj}^u d\Omega \tag{19}$$

Traditionally, ABAQUS finite element models are nonlinear and solved by Newton's method. The quadratic convergence rate in Newton's method is achieved by introducing the gradients matrix K_i^{NM}. However, there are some drawbacks when solving non-convex energy functional. The Jacobian matrix must be calculated and solved in the process. In the large models containing non-linear behaviours, the computational efforts are greatly increased. The quasi-Newton method enhances computational efficiency by approximating the Hessian matrix, thereby limiting the need for its explicit computation. This method leverages gradient information from previous iterations to construct an approximation of the Hessian, significantly reducing computational cost. By avoiding the direct calculation of second derivatives, the quasi-Newton method is particularly advantageous for large-scale problems, where the Hessian matrix can be prohibitively large. Additionally, this approach accelerates convergence compared to simple gradient descent methods and requires less memory, making it well-suited for high-dimensional parameter spaces. The Broyden-Fletcher-Goldfarb-Shanno (BFGS) algorithm [60] exemplifies these benefits by iteratively updating the Hessian approximation with gradient information, thereby achieving a balance between computational efficiency and convergence speed. The application of this quasi-Newton method is widely proven efficient in the publications [39,61–63]. The basic function of quasi-Newton method is to calculate a series of guess functions $\widetilde{K}_i^{NM}$ to the Jacobian matrix satisfying the secant condition, finally reaching the condition $\widetilde{K}_i^{NM} \approx K_i^{NM}$. In functional expression, the below formula is applied:

$$F^N(u_i^M) - F^N(u_{i-1}^M) = \widetilde{K}_i^{NM}(u_i^M - u_{i-1}^M) \tag{20}$$

The residual between two iterations can be formulated as:

$$\tau_i^N = F_i^N - F_{i-1}^N \tag{21}$$

Since the correction is denoted as ϖ_i^M, Eq. (21) is then written as:

$$\tau_i^N = \widetilde{K}_i^{NM}\varpi_i^M \tag{22}$$

Later, Matthies and Strange improved the efficiency of the BFGS method by creating a series of mathematical approximation, which retain the symmetry and positive definitions of $\widetilde{K}_i^{NM}$. The quasi-Newton method is embedded in the ABAQUS solver. The implementation of phase field method in dynamic elasto-plastic fracture is often computationally expensive. Therefore, the BFGS algorithm is applied to improve computational efficiency.

3.2. Virtual modelling technique in dynamic elasto-plastic fracture

The virtual modelling technique for the dynamic elasto-plastic fracture analysis is introduced in this section. The virtual modelling technique is capable to virtually predict the fracture responses without solving physics functional. In this study, the truncated T–spline kernel based extended support vector regression (X-SVR) method is employed to perform the training of virtual model. As a kernel sensitive approach, the performance of truncated T-spline kernel is validated in multiple random parameter regression. The spline functions can be considered as a set of piecewise polynomial functions by creating a smooth curve with preset points and are normally adopted in interpolation or smoothing techniques.

Developed from the original SVR or DrSVM [64–66], the X-SVR method utilizes the quadratic ε-insensitive loss function which does not penalize the errors within a certain threshold. Furthermore, the X-SVR method employs the kernel function to transform the raw data into a -dimensional space, resulting in a possible linear regression. In previous works [17,67], the X-SVR method is proven to be efficient and accurate in handling complex data structures or high-dimensional data.

The mapping function transforms the raw input data into a high dimensional space, making the linear regression possible. In X-SVR, the mapping function can be normally formulated as:

$$\mathbf{x}_i = \left[x_{i,1}, x_{i,2}, \cdots, x_{i,n}\right]^T \mapsto \widehat{d}(\mathbf{x}_i) = \begin{bmatrix} \chi(\mathbf{x}_1)^T\chi(\mathbf{x}_i) \\ \chi(\mathbf{x}_2)^T\chi(\mathbf{x}_i) \\ \vdots \\ \chi(\mathbf{x}_n)^T\chi(\mathbf{x}_i) \end{bmatrix} = \mathbf{D}(\mathbf{x}_i). \tag{23}$$

In Eq. (23), $\chi(\mathbf{x})$ denotes the mapping function and $\widehat{d}(\mathbf{x}_i)$ denotes the empirical kernelized vector. The transforming kernelized mapping function are written as:

$$\mathbf{D}(\mathbf{x}_i) = \begin{bmatrix} \mathbf{D}(\mathbf{x}_1,\mathbf{x}_1) & \mathbf{D}(\mathbf{x}_1,\mathbf{x}_2) & \cdots & \mathbf{D}(\mathbf{x}_1,\mathbf{x}_j) \\ \mathbf{D}(\mathbf{x}_2,\mathbf{x}_1) & \mathbf{D}(\mathbf{x}_2,\mathbf{x}_2) & \cdots & \mathbf{D}(\mathbf{x}_2,\mathbf{x}_j) \\ \vdots & \vdots & \ddots & \vdots \\ \mathbf{D}(\mathbf{x}_j,\mathbf{x}_1) & \mathbf{D}(\mathbf{x}_j,\mathbf{x}_1) & \cdots & \mathbf{D}(\mathbf{x}_j,\mathbf{x}_j) \end{bmatrix} \tag{24}$$

Then, the original system inputs can be transformed into high dimensional space by the mapping function. In the high-dimensional space, the regression problem will be solved using the following optimization algorithm:

$$\begin{aligned} &\min_{\mathbf{p}_x,\mathbf{q}_x,\alpha,\rho,\widehat{\rho}} : \frac{\iota_1}{2}\left(\| \mathbf{r}_x\|_2^2 + \| \mathbf{t}_x \|_2^2\right) + \iota_2\mathbf{e}_j^T(\mathbf{r}_x + \mathbf{t}_x) + \frac{\chi}{2}\left(\rho^T\rho + \widehat{\rho}^T\widehat{\rho}\right) \\ &s.t.\begin{cases} \sigma\mathbf{e}_j + \rho \geq \mathbf{M}_{train}(\mathbf{r}_x - \mathbf{t}_x) - \alpha\mathbf{e}_j - \mathbf{y}_{train} \\ \sigma\mathbf{e}_j + \widehat{\rho} \geq \mathbf{y}_{train} - \mathbf{M}_{train}(\mathbf{r}_x - \mathbf{t}_x) + \alpha\mathbf{e}_j \\ \qquad\qquad \mathbf{r}_x, \mathbf{t}_x, \rho, \widehat{\rho} \geq 0^j \end{cases} \end{aligned} \tag{25}$$

here χ is the penalty parameter; σ is the parameter identifying the acceptable deviation; $\mathbf{e}_j$ is a unit vector; $\mathbf{r}_x$, $\mathbf{t}_x$ are the positive parameters normal to the hyperplane; ρ, $\widehat{\rho}$ are the slack variables for excess deviations and the tunning variables for feature selection are denoted as ι_1, ι_2.

The optimization problem is then further simplified into a quadratic programming problem as:

$$\begin{aligned} &\min_{\mathbf{y}_{train},\lambda} : \frac{1}{2}\left(\mathbf{r}_x^T\widehat{\mathbf{R}}_x\mathbf{r}_x + \alpha^2\right) + \iota_2\mathbf{z}_x^T\mathbf{n}_x \\ &s.t.\left(\widehat{\mathbf{A}}_x + \mathbf{I}_{4j\times 4j}\right)\mathbf{n}_x + \left(\omega\mathbf{I}_{4j\times 4j} + \chi\widehat{\mathbf{D}}_x\right)\widehat{\mathbf{e}}_x + \widehat{\mathbf{g}}_x \geq \mathbf{0}_{4j} \end{aligned} \tag{26}$$

$$\begin{aligned} &\min_{\varsigma_x} : \frac{1}{2}\tau_x^T\mathbf{V}_x\tau_x - \mathbf{s}_x^T\tau_x \\ &s.t.\tau_x \geq \mathbf{0}_{4j} \end{aligned} \tag{27}$$

where the identity matrix is $\mathbf{I}_{4j\times 4j}$, the detailed explanation of corresponding matrix vector can be found in the former publications [17]. Given the global minimum solution h_x^*, the expression of the related variables can be written as:

$$\mathbf{n}_x = \widehat{\mathbf{Q}}_x^{-1}\left(\left(\widehat{\mathbf{A}}_x + \mathbf{I}_{4j\times 4j}\right)^T h_x^* - \beta_2\mathbf{z}_x\right) \tag{28}$$

$$\chi = \widehat{\mathbf{e}}_x^T\widehat{\mathbf{D}}_x h_x^* \tag{29}$$

Therefore, the overall governing expression of X-SVR algorithm can be proposed as:

$$\begin{cases} \mathbf{r}_x - \mathbf{t}_x = \mathbf{n}_x(1:j) - \mathbf{n}_x(j+1:2j) \\ \widehat{f}(\mathbf{x}) = (\mathbf{r}_x - \mathbf{t}_x)^T\widehat{d}(\mathbf{x}) - \widehat{\mathbf{e}}_x^T\widehat{\mathbf{D}}_x h_x^* \end{cases} \tag{30}$$

Recently, the truncated T–spline polynomial kernel function is based on T-splines and achieved by the truncation mechanism. This

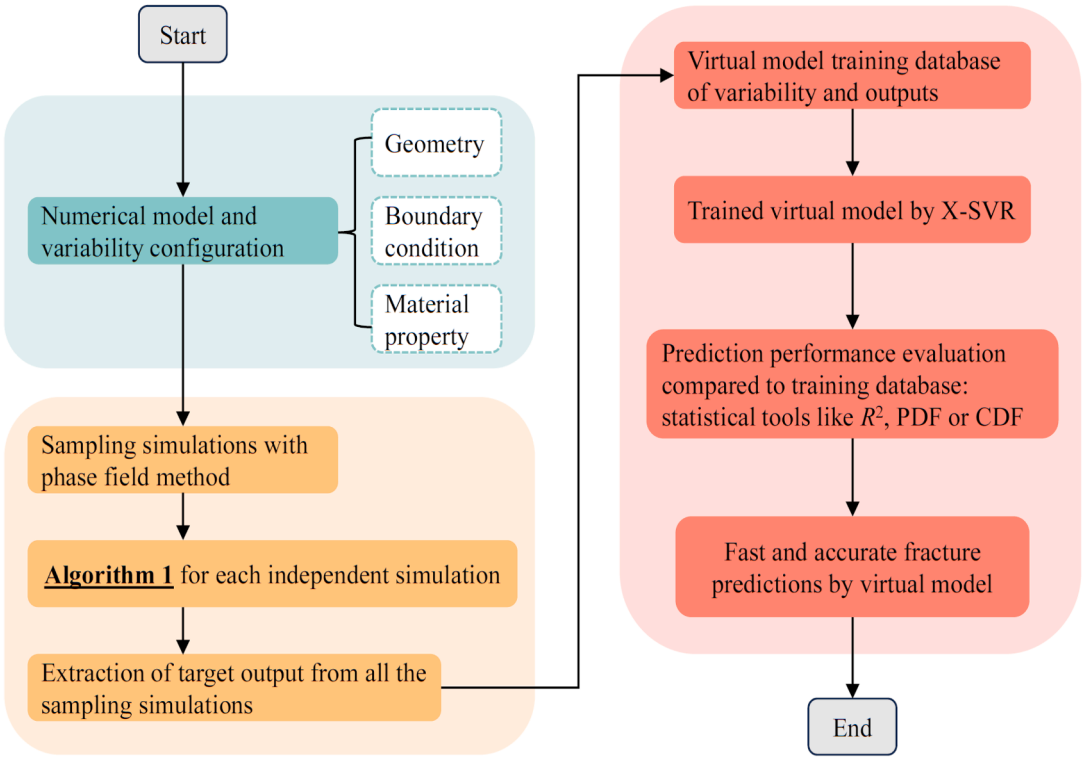

Algorithm 1: Dynamic fracture analysis in elasto-plastic material by phase field method

Assumption: total time step = n;

Initialization: $u_{i=0}^{j=0}, H_{i=0}^{j=0}, \emptyset_{i=0}^{j=0}$

For every successive time step **do**

Guess the strain and stress initially

Calculate σ_{mises}

if $\sigma_{mises} < \sigma_{y0}$, pure elastic

else calculate hydrostatic stresses and flow rules

Solve the governing equation

$$\begin{bmatrix} S_n^u(\eta_j^R) & 0 \\ 0 & (1+\alpha)K_n^d(\eta_j^R) \end{bmatrix} \begin{bmatrix} u_{n+\Delta t}(\eta_j^R) \\ \phi_{n+\Delta t}(\eta_j^R) \end{bmatrix} = - \begin{bmatrix} r_n^u(\eta_j^R) \\ \alpha r_{n-1}^d(\eta_j^R) - (1+\alpha) r_n^d(\eta_j^R) \end{bmatrix}$$

while not converged **do** j = j + 1

Update the displacement field u_n^{j+1}, history field H_n^{j+1} and phase field $\emptyset_n^{j+1}$ in sequence

End

Fig. 3. Flow chart of virtual modelling technique for non-deterministic dynamic fracture analysis in elasto-plastic materials.

mechanism equips the traditional T-splines with reduced support overlapping and better performance. With in X-SVR algorithm, the truncated T–spline polynomial kernel function is defined as:

$$\mathbf{T}_{t-spline}(x) = \sum_{i=0}^{n} C_i \cdot B_i(x) \tag{31}$$

and,

$$B_i(x) = \frac{x - x_i}{x_{i+k} - x_i} \cdot \mathrm{B}_{i-1}(x) + \frac{x_{i+k+1} - x_i}{x_{i+k+1} - x_{i-1}} \mathrm{B}_{i-1}(x+1) \tag{32}$$

where $C_i$are the scalar values that weight the contribution of each basis function, B_i are the basis functions, $x_i x_{i+1,\ldots,} x_{i+k+1}$ are the knot values, and k is the order of spline.

The general algorithm of the proposed virtual modelling technique in dynamic elasto-plastic fracture is shown in Fig. 3. The final step is to evaluate the performance of the prediction by virtual model. The statistical error estimation parameter R^2 is utilized between the results of repetitive sampling simulations and virtual model predictions.

$$R^2 = 1 - \frac{\sum_{i=1}^{j} (\widehat{f}i - y_i)^2}{\sum_{i=1}^{j} (\overline{y} - y_i)^2} \tag{33}$$

where $\widehat{f}$ is the virtual model's predicted results, y and $\overline{y}$ are the sampling simulation results and their mean values.

4. Numerical verification and examples

In order to demonstrate the implementation of the proposed non-deterministic phase field modelling technique, two real-world 3D examples are performed. In each example, the crack propagation processes are compared to the recorded damage to verify the effectiveness. Furthermore, the numerical efficiency is also corroborated in this chapter.

4.1. Roller coaster column

In July 2023, one support column of the famous roller coaster in USA, Fury 325, was found broken during operation [68] and the crack totally went through the column, as shown in Fig. 4. The roller coaster was then shut down for repair. This public crisis alerted people to keep tighter monitoring of the structural health of similar equipment. Given by this event, the first numerical example of the non-deterministic phase field modelling in elasto-plastic material studies the roller coaster column.

The numerical column model takes a similar geometry to the real one. The model consists of two circular tubes and the horizontal connection beam is in the H section. The boundary conditions and geometric information is shown in Fig. 5 (a). Assuming that the column is made up of structural steel, the material properties are chosen as: Young's modulus $E = 200\text{GPa}$, Poisson ratio $\nu = 0.29$, initial yield stress $\sigma_{y0} = 300\text{MPa}$, density $\rho = 7850\text{kg}/\text{m}^3$ and critical energy release rate $G_c = 100\text{MPa} \cdot \text{mm}$. In this case, the linear hardening law is adopted for simplicity and the hardening modulus is selected as $H = 1000\text{MPa}$. The load is directly applied on the cross section of H horizontal beam, which simulates the real-world working condition of roller coaster. For the dynamic fracture analysis, three load phases simulating different passenger loads are implemented. The load history is demonstrated in Fig. 5 (c).

The model is first tested in deterministic condition to verify the accuracy of implemented codes. C3D4 element in Abaqus is applied for its efficiency in generating meshes from arbitrary 3D geometry. In this implementation, a total of 59,401 elements are used, and the mesh is refined in the potential crack propagation area, as shown in Fig. 5 (b). A tiny crack of 2 mm is located on the joint of the support

Fig. 4. Damaged roller coaster column in Fury 325.

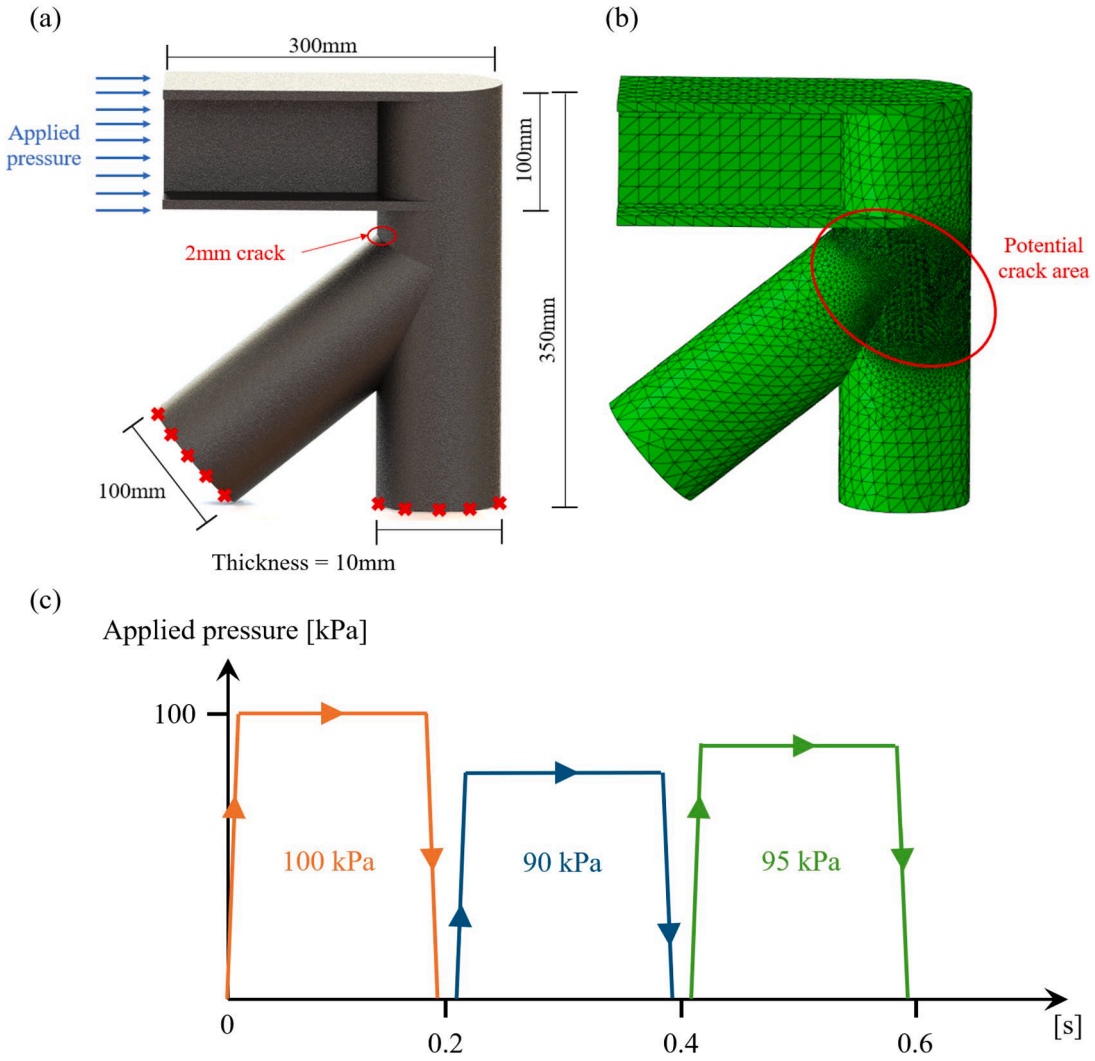

Fig. 5. (a) Geometry and boundary conditions. (b) Meshed numerical model. (c) Load history.

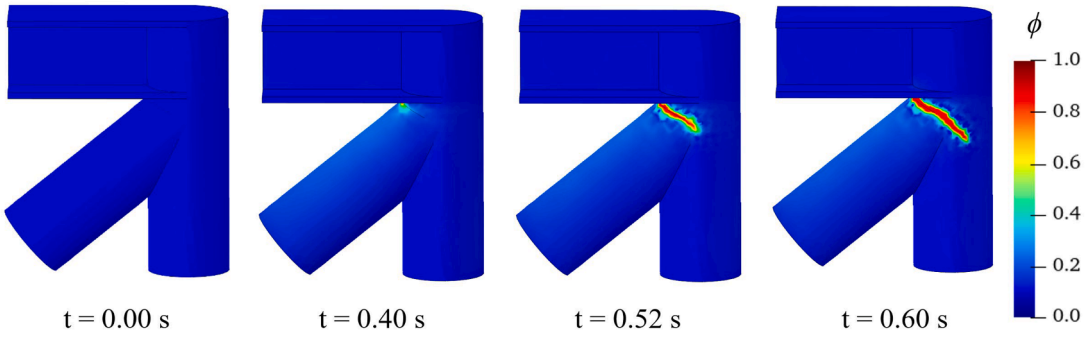

Fig. 6. Crack propagation plots at different times.

column. The total simulation time is 0.6 s and 6000 fixed time steps are adopted. The plots in Fig. 6 demonstrate the crack propagation process. Compared to the crack patten in Fig. 4, it can be verified that the implementation of phase field modelling of dynamic fracture in elasto-plastic materials is appropriate.

After the verification, non-deterministic parameters are proposed considering the existence of variability. Amongst these non-

Table 2
Statistical information of non-deterministic material properties and loads in roller coaster column example.

Non-deterministic parameters		Distribution type	Mean	Standard deviation	Range
Material properties	Young's modulus E [GPa]	Normal [69]	200	2	/
	Poisson ratio	Beta [70]	0.29	0.005	/
	Yield stress σ_{y0} [MPa]	Log-normal	300	10	/
	Density ρ [kg/m^3]	Normal	7850	150	
	Critical energy release rate G_c[MPa•mm]	Uniform [71]	100	/	[95.00, 105.00]
Applied pressure	Load phase 1 [kPa]	Normal	100	1	/
	Load phase 2 [kPa]	Uniform	90	/	[88, 92]
	Load phase 3 [kPa]	Log-normal	95	1	/

deterministic parameters in Table 2, different distribution types are adopted to simulate various scenarios in real-world applications.

Because of the complexity and long computational time in solving dynamic elasto-plastic fracture problems, 300 times simulations based on the non-deterministic parameters are performed using BFGS algorithm. The outputs of these simulations are adopted as sampling simulations in virtual model training process. It can be found in Fig. 6 that the crack propagation speeds up after the crack reaches the column joint ($t = 0.52$ s). Therefore, the first prediction target of virtual model implementation is the time when crack reaches the joint. For the existence of non-deterministic parameters, the time varies amongst 300 independent numerical tests. The total running time of 300 simulations is more than 10 days on the platform by National Computational Infrastructure (NCI) with high-performance computers. After completion, then the virtual model training process costs 1 day to train the adequate virtual model based on i7-12700K CPU and 128G RAM. Given the detailed information about variabilities and outputs, the virtual model can be trained with X-SVR algorithm by building a virtual governing relationship between them instead of the physical formulations. Once the virtual model is generated, the fracture prediction can be obtained within 1 s. The training performance of the first prediction target can be found in Fig. 7. The probability density function (PDF) and cumulative distribution function (CDF) plots are provided to demonstrate the virtual model prediction performance compared to the sampling simulations. Furthermore, the relative errors are calculated in Fig. 7 (c). In these figures, the prediction by the virtual model is marked in red points while the sampling data is marked in black solid line. It is approved that the prediction performance is excellent.

Moreover, another prediction target is set as the total crack length to comprehensively demonstrate the effectiveness of the virtual modelling technique. The training performance is compared with repetitive tests in Fig. 8.

Similarly, after the crack propagation data is collected, the prediction of final crack location can be performed. In this case, the geometry location of crack tip at the end of simulation is extracted and trained by the X-SVR algorithm to generate a virtual model respectively. The training performance shows that the virtual model prediction can accurately simulate the results of phase field method, meaning that the virtual model could be adopted in further numerical study. Continuously, in Fig. 9, the probability density functions of x and y direction is demonstrated. These heat maps are provided by the well-trained virtual models. The crack tip locations are also shown in Fig. 9. With this kind of heat-map, the virtual model can be applied to guide the design process in order to prevent similar crack propagation by improving the fracture resistance in relative area.

4.2. Tooth replacement implant

Inspired by medical records about tooth implant fractures, the second numerical example focuses on the dynamic fracture during the service life of tooth implant. The service load includes severe loading conditions when people chew some hard food like bones. In the numerical simulation, only the metal alloy parts including abutment and implant body are modelled in Fig. 10.

The 3D model of tooth implant is constructed with respect to geometry illustrated in Fig. 11. The load is applied as the combined displacement along x and z directions. A tiny 0.1 mm pre-crack is located in the joint part to simulate decay in normal usage. The mesh of numerical model is refined in the potential crack area around the initial tiny crack. Two materials are selected in this example to show how the material property affects the fracture process in dynamic cases. The numerical model is made up of two different

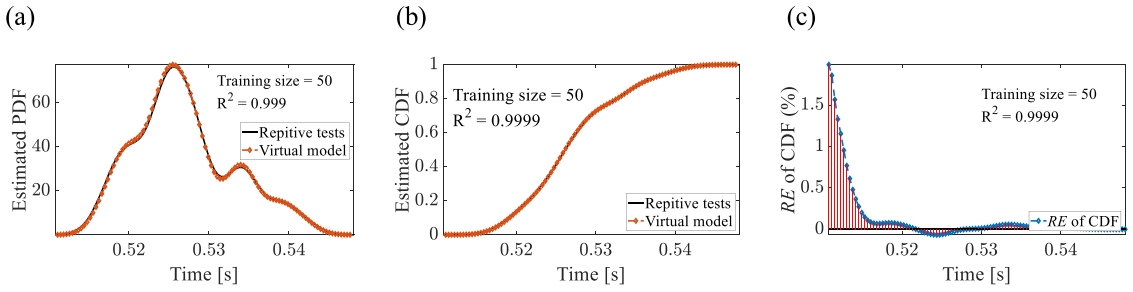

Fig. 7. Comparison of the time when crack reaches the joint by virtual model and phase field method: (a) estimated PDF plot; (b) estimated CDF plot; (c) relative error of CDF.

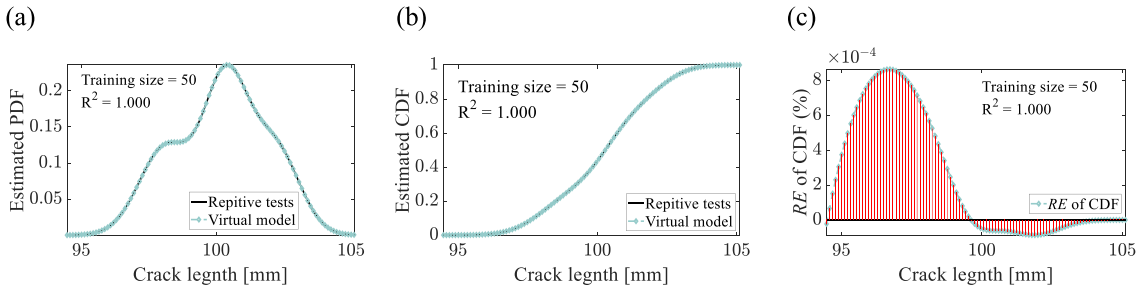

Fig. 8. Comparison of the final crack length by virtual model and phase field method: (a) estimated PDF plot; (b) estimated CDF plot; (c) relative error of CDF.

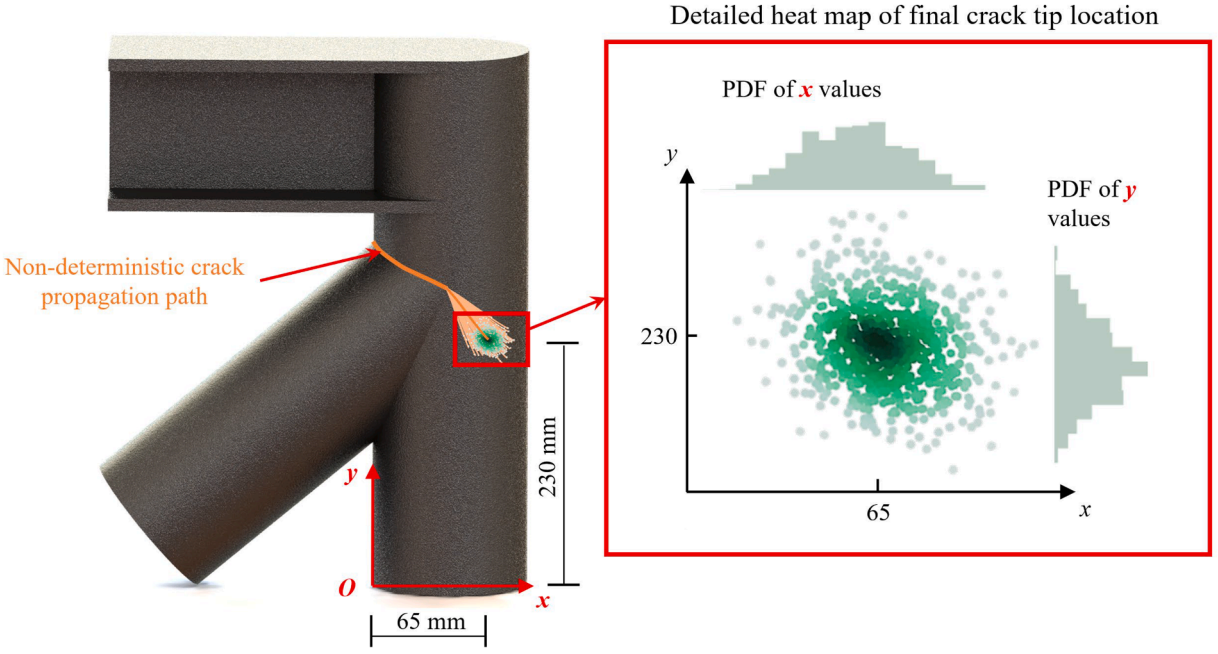

Fig. 9. Heat map of predicted crack tip location.

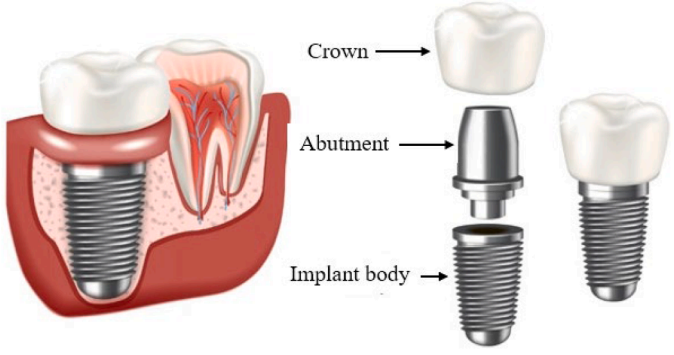

Fig. 10. Tooth replacement implant parts.

materials, stainless steel, and titanium, to compare their performance in service life. The material properties of stainless steel are: Young's modulus $E = 200\text{GPa}$, Poisson ratio $\nu = 0.29$, initial yield stress $\sigma_{y0} = 300\text{MPa}$, density $\rho = 7850\text{kg}/\text{m}^3$ and critical energy release rate$G_c = 150\text{MPa} \cdot \text{mm}$. Additionally, the material properties of titanium alloy are chosen as: Young's modulus $E = 116\text{GPa}$,

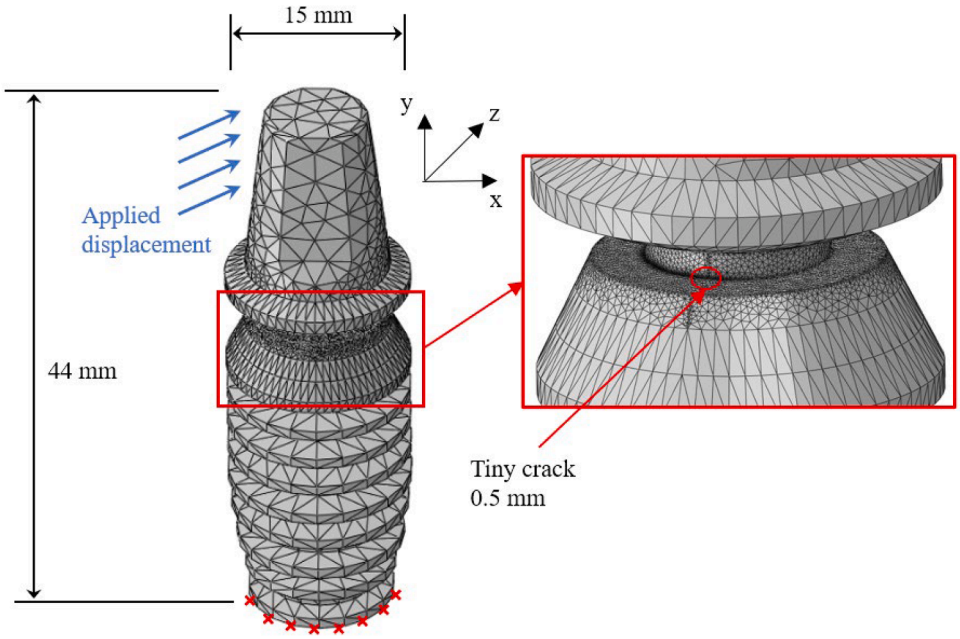

Fig. 11. Numerical model and boundary conditions of tooth implant.

Poisson ratio$\nu = 0.33$, initial yield stress $\sigma_{y0} = 400$MPa, density $\rho = 4500\text{kg}/\text{m}^3$ and critical energy release rate$G_c = 100\text{MPa} \cdot \text{mm}$. The linear hardening law is adopted for simplicity and the universal hardening modulus is selected as $H = 1000$MPa. The total displacement is 2 mm within 1 s.

For the verification purposes, the numerical simulation results are compared to medical records in Fig. 12. It is clear that the crack propagates from the initial tiny crack and extends along the connection surface. The result shed light for further investigation of the dynamic fracture behaviour of tooth implant. Considering the unexpected service condition, the uncertainties regarding external loads are added to the non-deterministic material property parameters. The materials of tooth implants vary from stainless steel to titanium. In this numerical example, the detailed information of considered uncertainties is listed in Table 3.

After the settings of uncertainties, 300 times sampling simulations of each material are performed using BFGS algorithm. To obtain a good understanding of fracture responses, the evaluation of crack length at the end of simulation is performed. Subsequently, two virtual models are trained separately in each material to demonstrate the influence of material property especially in elasto-plastic materials. In this case, the total running times are 11 days for stainless steel and 12 days for titanium on NCI. After that, then the virtual model training process costs 1 day for both materials to train the adequate virtual models. With the trained virtual models, the fracture responses can be predicted within seconds. In Figs. 13 and 14, the statistical information of training performance including PDF plots, CDF plots and relative errors shows that the virtual models can predict the fracture responses accurately for both materials.

Before conducting the sensitivity analysis, the determination of the material is crucial. In practical applications, titanium is preferred over stainless steel for tooth medical implants due to its lightweight nature, biocompatibility, and high strength. These attributes make titanium an ideal choice for medical implants. Utilizing the well-trained virtual models, we have evaluated the fracture response performance of both materials. The final crack tip locations are illustrated in Fig. 15, and a detailed comparison of crack propagation between the two materials is provided in Table 4. Additionally, Fig. 16 compares the difference in crack propagation between titanium and stainless steel. The results clearly indicate that implants made of titanium exhibit superior fracture durability compared to those made of stainless steel. Specifically, the initiation of cracks in titanium implants is significantly delayed under identical load conditions. This delay in crack initiation underlines the material's higher resilience and better long-term durability in medical applications. Based on these findings, it is evident that titanium should be the material of choice for dental implants in clinical practice. The superior properties of titanium not only enhance the longevity of the implants but also contribute to improved patient outcomes by reducing the likelihood of implant failure.

Since the material has been determined as titanium, the sensitivity analysis can be conducted to guide designers and engineers on how to improve the fracture performance in medical tooth implant. The virtual models for both materials are well trained based on the information, then the sensitivity analysis is performed. Sensitivity analysis enables the understanding of the relationship between different factors and their contribution to the overall fracture behaviour of the model. To achieve this, the virtual model is utilized to predict the fracture responses with assigned variation (5 %). The numerical results are summarized in Table 5. In Fig. 17, amongst all the uncertainties, the initial yield stress is the most influential factor affecting fracture performance, whereas Young's modulus also plays a critical role as a determinative parameter in dynamic elasto-plastic fracture. Through this sensitivity analysis, the virtual modelling technique has shown the capability of guiding structural design process by telling the most critical material parameters from various non-deterministic parameters. Therefore, engineers can specifically improve existing products or structures to achieve superior

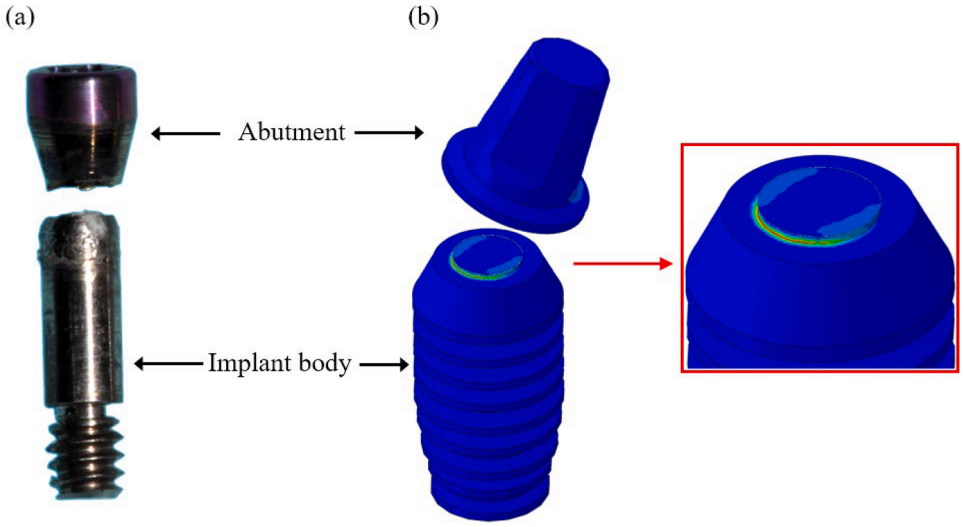

Fig. 12. Tooth implant fracture: (a) photo from medical record [72], (b) numerical simulation.

Table 3
Statistical information of non-deterministic material properties and load in tooth implant example.

Non-deterministic parameters		Distribution type	Mean	Standard deviation	Range
Material properties of stainless steel	Young's modulus E [GPa]	Log-normal	200	2	/
	Poisson ratio	Beta	0.29	0.005	/
	Yield stress σ_{y0} [MPa]	Normal	300	10	/
	Density ρ [kg/m^3]	Log-normal	7850	150	
	Critical energy release rate G_c[MPa•mm]	Uniform	150	/	[145.00, 155.00]
Material properties of titanium alloy	Young's modulus E [GPa]	Log-normal	116	2	/
	Poisson ratio	Beta	0.33	0.005	/
	Yield stress σ_{y0} [MPa]	Normal	400	10	/
	Density ρ [kg/m^3]	Log-normal	4500	150	
	Critical energy release rate G_c[MPa•mm]	Uniform	100	/	[94.00, 104.00]
Applied load	x-direction [mm]	Normal	2	0.1	/
	z-direction [mm]	Log-normal	0.1	0.005	/

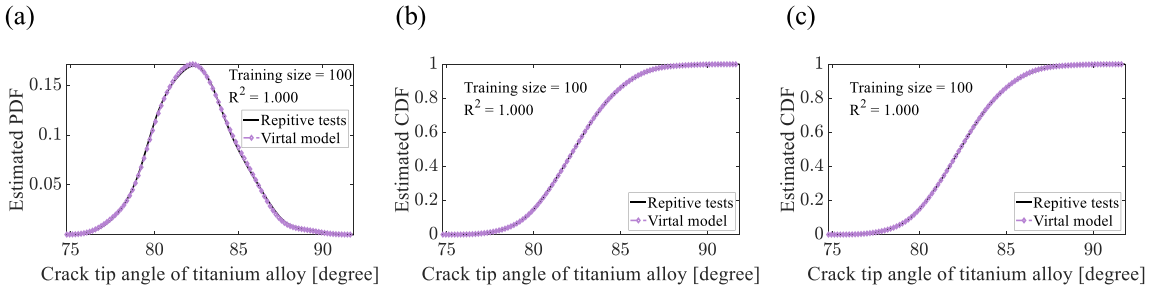

Fig. 13. Comparison of the crack tip angle of titanium alloy: (a) estimated PDF plot; (b) estimated CDF plot; (c) relative error of CDF.

crack resistance performance.

5. Conclusion

In conclusion, this study introduces a pioneering framework for analysing dynamic elasto-plastic fracture in materials under non-deterministic conditions. The integration of the phase field method and the innovative virtual modelling algorithm enables this framework to predict fracture responses efficiently and accurately. This approach is proven in handling high-dimensional, nonlinear problems, creating a virtual model that adeptly links fracture responses with various uncertain parameters.

The phase field method was chosen for its outstanding capability to tackle complex fracture problems, providing reliable data for

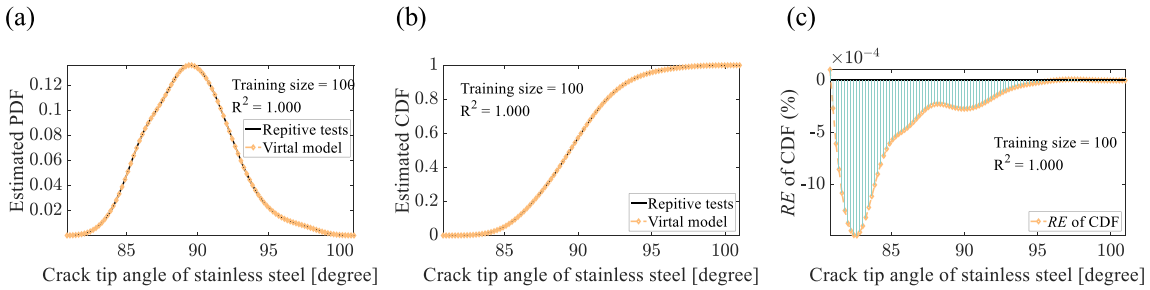

Fig. 14. Comparison of the crack tip angle of stainless steel: (a) estimated PDF plot; (b) estimated CDF plot; (c) relative error of CDF.

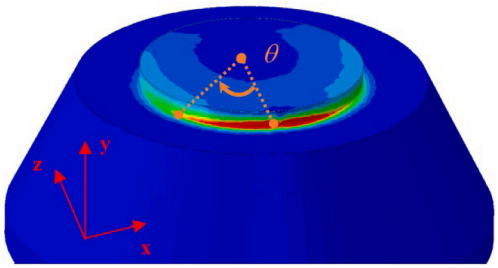

Fig. 15. Measurement of final crack tip location θ [degree].

Table 4
Comparison of final crack tip location between two materials.

Material	Stainless steel	Titanium
Crack tip location [degree]	89.114	82.478

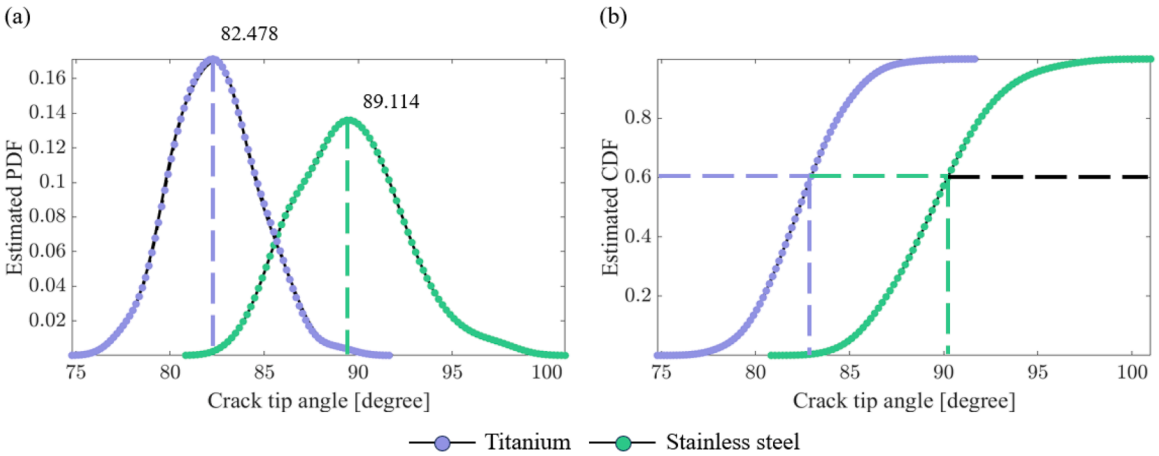

Fig. 16. Comparison of statistical information between two materials: (a) estimated PDF plot; (b) estimated CDF plot.

training, and validating the virtual model. The framework's implementation to dynamic elasto-plastic fracture problems was validated through two practical engineering examples. These numerical examples highlight the framework's ability to deliver precise, real-time predictions of crack propagation even with multiple uncertainties. This makes it not only feasible but also practical for contemporary numerical dynamic fracture simulations. This framework addresses and overcomes several limitations of traditional phase field method simulations. It reached a balance between accurate modelling and computational efficiency, reducing the typically high computational costs associated with detailed simulations without losing accuracy. This efficiency makes the framework suitable for various extensions, such as sensitivity analysis and design optimization. Accurate prediction of dynamic fracture responses under uncertain conditions can lead to more resilient and safer designs. Comprehensive explanations of both deterministic and non-

Table 5
Sensitivity analysis of uncertainties on crack propagation in titanium tooth implant.

Uncertainties	Crack tip angle [degree]		Maximum variation at ±5 % mean value [%]
	95 % mean value	105 % mean value	
Young's modulus [GPa]	80.488	84.238	2.413
Poisson ratio	81.771	82.680	0.857
Yield stress [MPa]	79.444	85.935	4.191
Density [kg/m^3]	81.549	83.504	1.244
Critical energy release rate [MPa•mm]	80.917	83.598	1.893
Applied load x [mm]	82.343	82.600	0.164
Applied load z [mm]	82.059	82.942	0.563

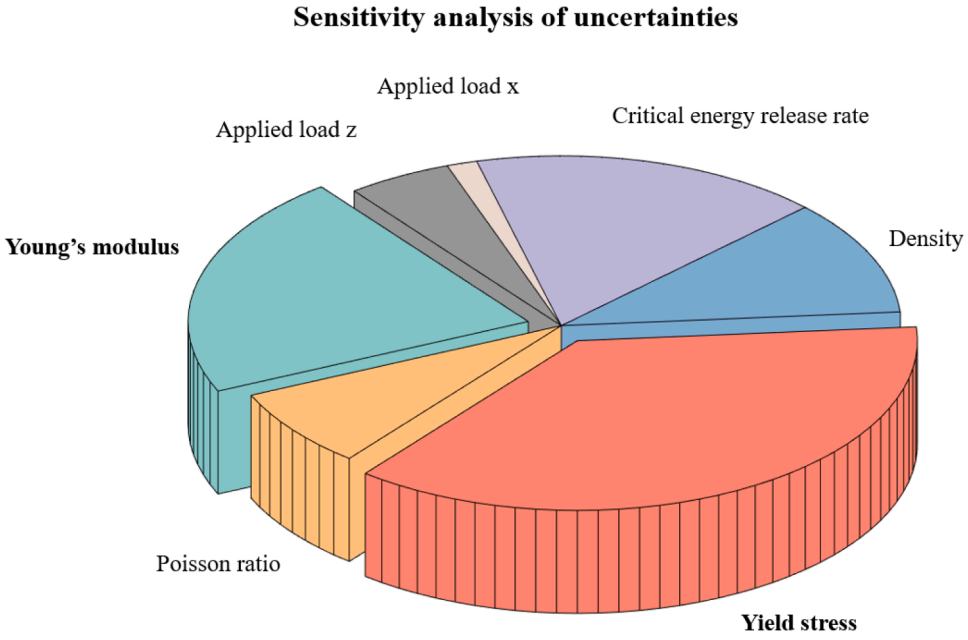

Fig. 17. Comparison of the influence of uncertainties in titanium tooth implant.

deterministic fracture analyses by detailed numerical examples and verifications, provide a deep understanding of this innovative computational framework.

This study offers a powerful tool for engineers and researchers to tackle complex dynamic fracture problems in elasto-plastic materials. This framework holds promise for enhancing structural safety, guiding preventive design, and informing real-time maintenance strategies, ultimately contributing to more robust and reliable engineering solutions.

CRediT authorship contribution statement

Yiyang Liu: Writing – original draft, Validation, Software, Methodology, Formal analysis, Conceptualization. **Yuan Feng:** Writing – review & editing, Supervision, Software, Methodology, Conceptualization. **Zhangming Wu:** Writing – review & editing, Software, Investigation, Conceptualization. **Mehrisadat Makki Alamdari:** Writing – review & editing, Software, Investigation, Conceptualization. **Di Wu:** Supervision, Software, Methodology, Investigation. **Zhen Luo:** Writing – review & editing, Software, Methodology, Conceptualization. **Xiaojun Chen:** Software, Methodology, Funding acquisition. **Wei Gao:** Writing – review & editing, Supervision, Funding acquisition, Conceptualization.

Declaration of competing interest

The authors declare that they have no known competing financial interests or personal relationships that could have appeared to influence the work reported in this paper.

Data availability

No data was used for the research described in the article.

Acknowledgments

This research is fully funded by Australia Research Council projects IH210100048, IH200100010, DP240102559 and DP210101353. The author Yiyang Liu is funded by Australian Government Research Training Program Scholarship (RTP).

References

[1] A.J. Brunner, 8 - Fracture mechanics of polymer composites in aerospace applications, P. Irving, C. Soutis (Eds.). Polymer Composites in the Aerospace Industry, 2nd ed., Woodhead Publishing, 2020, pp. 195–252, https://doi.org/10.1016/B978-0-08-102679-3.00008-3.
[2] A. Lambers, B. Rieger, A. Kop, P. D'Alessandro, P. Yates, Implant fracture analysis of the TFNA proximal femoral nail, J. Bone Jt. Surg. Am. 101 (2019) 804–811, https://doi.org/10.2106/jbjs.18.00997.
[3] Y. Feng, D. Wu, M.G. Stewart, W. Gao, Past, current and future trends and challenges in non-deterministic fracture mechanics: a review, Comput. Methods Appl. Mech. Eng. 412 (2023) 116102, https://doi.org/10.1016/j.cma.2023.116102.
[4] S. Abrari Vajari, M. Neuner, P.K. Arunachala, C. Linder, Investigation of driving forces in a phase field approach to mixed mode fracture of concrete, Comput. Methods Appl. Mech. Eng. 417 (2023) 116404, https://doi.org/10.1016/j.cma.2023.116404.
[5] Y. Yu, B. Dong, A. Liu, J. Fu, W. Gao, Phase field to fracture analysis on engineered cementitious composites under complex stress states, Int. J. Mech. Sci. 261 (2024) 108672, https://doi.org/10.1016/j.ijmecsci.2023.108672.
[6] Y. Yu, B. Dong, A. Liu, J. Fu, W. Gao, A unified phase field solution to fracture analyses on (pseudo) elastoplastic solids and structures, Theoret. Appl. Fract. Mech. 129 (2024) 104225, https://doi.org/10.1016/j.tafmec.2023.104225.
[7] B. Dong, Y. Yu, W. Gao, G. Zhao, A novel method for chloride-induced corrosion analysis incorporating consistent ionic diffusivity and concrete resistivity, Constr. Build. Mater. 365 (2023) 129941, https://doi.org/10.1016/j.conbuildmat.2022.129941.
[8] B. Dong, Y. Yu, Y. Feng, D. Wu, G. Zhao, A. Liu, W. Gao, Robust numerical solution for assessing corrosion of reinforced concrete structures under external power supply, Eng. Struct. 294 (2023) 116724, https://doi.org/10.1016/j.engstruct.2023.116724.
[9] X. Sun, Y. Zhang, Adaptive stochastic isogeometric analysis for nonlinear bending of thin functionally graded shells with material uncertainties, Comput. Methods Appl. Mech. Eng. 417 (2023) 116407, https://doi.org/10.1016/j.cma.2023.116407.
[10] Y. Tian, Q. Li, Y. Feng, Z. Luo, D. Ruan, W. Gao, Nonlinear dynamic analysis of the graphene platelets reinforced porous plate with magneto-electro-elastic sheets subjected to impact load, Nonlinear Dyn. 112 (2024) 1661–1690, https://doi.org/10.1007/s11071-023-09093-3.
[11] T. Zhang, T.Yu Hirshikesh, C. Xing, S. Natarajan, An adaptive dynamic phase-field method using the variable-node elements for cohesive dynamic fracture, Comput. Methods Appl. Mech. Eng. 416 (2023) 116390, https://doi.org/10.1016/j.cma.2023.116390.
[12] O. Mayorquin, Large Crack Spotted in Roller Coaster Prompts Its Shutdown. https://www.nytimes.com/2023/07/02/us/north-carolina-roller-coaster-closed.html.
[13] P. Schutz, Cracked Lake Shore Drive Bridge Reopens. https://news.wttw.com/2019/02/12/cracked-lake-shore-drive-bridge-reopens, 2019.
[14] J.F. Knott, Fundamentals of Fracture Mechanics, Gruppo Italiano Frattura, 1973.
[15] M.F. Kanninen, C.H. Popelar, Advanced Fracture Mechanics, Oxford University Press, 1985.
[16] L.B. Freund, Dynamic Fracture Mechanics, Cambridge University Press, Cambridge, 1990, https://doi.org/10.1017/CBO9780511546761.
[17] Y. Feng, Q. Wang, X. Chen, D. Wu, W. Gao, Virtual modelling technique for geometric-material nonlinear dynamics of structures, Struct. Saf. 100 (2023) 102284, https://doi.org/10.1016/j.strusafe.2022.102284.
[18] J. Fineberg, M. Marder, Instability in dynamic fracture, Phys. Rep. 313 (1999) 1–108, https://doi.org/10.1016/S0370-1573(98)00085-4.
[19] B. Bourdin, C.J. Larsen, C.L. Richardson, A time-discrete model for dynamic fracture based on crack regularization, Int. J. Fract. 168 (2011) 133–143, https://doi.org/10.1007/s10704-010-9562-x.
[20] W. Hu, Y.D. Ha, F. Bobaru, Peridynamic model for dynamic fracture in unidirectional fiber-reinforced composites, Comput. Methods Appl. Mech. Eng. 217-220 (2012) 247–261, https://doi.org/10.1016/j.cma.2012.01.016.
[21] J.H. Song, H. Wang, T. Belytschko, A comparative study on finite element methods for dynamic fracture, Comput. Mech. 42 (2008) 239–250, https://doi.org/10.1007/s00466-007-0210-x.
[22] Q. Shi, H. Yu, L. Guo, L. Hao, K. Huang, A phase field model with plastic history field for fracture of elasto-plastic materials, Eng. Fract. Mech. 268 (2022) 108447, https://doi.org/10.1016/j.engfracmech.2022.108447.
[23] J. Fang, C. Wu, T. Rabczuk, C. Wu, C. Ma, G. Sun, Q. Li, Phase field fracture in elasto-plastic solids: Abaqus implementation and case studies, Theoret. Appl. Fract. Mech. 103 (2019) 102252, https://doi.org/10.1016/j.tafmec.2019.102252.
[24] Y. Tian, Q. Li, Y. Feng, Y. Yu, D. Wu, X. Chen, W. Gao, Nonlinear dynamic analysis of the functionally graded graphene platelets reinforced porous plate under moving mass, Thin Walled Struct. 183 (2023) 110363, https://doi.org/10.1016/j.tws.2022.110363.
[25] Y. Feng, M.M. Alamdari, D. Wu, Z. Luo, D. Ruan, T. Egbelakin, X. Chen, W. Gao, Virtual modelling aided safety assessment for ductile structures against high-velocity impact, Eng. Struct. 301 (2024) 117373, https://doi.org/10.1016/j.engstruct.2023.117373.
[26] N. Sukumar, N. Moës, B. Moran, T. Belytschko, Extended finite element method for three-dimensional crack modelling, Int. J. Numer. Methods Eng. 48 (2000) 1549–1570, https://doi.org/10.1002/1097-0207(20000820)48:11<1549::AID-NME955>3.0.CO;2-A.
[27] M. Jirásek, M. Bauer, Numerical aspects of the crack band approach, Comput. Struct. 110-111 (2012) 60–78, https://doi.org/10.1016/j.compstruc.2012.06.006.
[28] G.A. Francfort, J.J. Marigo, Revisiting brittle fracture as an energy minimization problem, J. Mech. Phys. Solids 46 (1998) 1319–1342, https://doi.org/10.1016/S0022-5096(98)00034-9.
[29] B. Bourdin, G.A. Francfort, J.J. Marigo, Numerical experiments in revisited brittle fracture, J. Mech. Phys. Solids 48 (2000) 797–826, https://doi.org/10.1016/S0022-5096(99)00028-9.
[30] B. Bourdin, G.A. Francfort, J.J. Marigo, The variational approach to fracture, J. Elast. 91 (2008) 5–148, https://doi.org/10.1007/s10659-007-9107-3.
[31] C. Miehe, F. Welschinger, M. Hofacker, Thermodynamically consistent phase-field models of fracture: Variational principles and multi-field FE implementations, Int. J. Numer. Methods Eng. 83 (2010) 1273–1311, https://doi.org/10.1002/nme.2861.
[32] M. Ambati, T. Gerasimov, L. De Lorenzis, A review on phase-field models of brittle fracture and a new fast hybrid formulation, Comput. Mech. 55 (2015) 383–405, https://doi.org/10.1007/s00466-014-1109-y.
[33] M.A. Msekh, J.M. Sargado, M. Jamshidian, P.M. Areias, T. Rabczuk, Abaqus implementation of phase-field model for brittle fracture, Comput. Mater. Sci. 96 (2015) 472–484, https://doi.org/10.1016/j.commatsci.2014.05.071.
[34] S. Nagaraja, M. Elhaddad, M. Ambati, S. Kollmannsberger, L. De Lorenzis, E. Rank, Phase-field modeling of brittle fracture with multi-level hp-FEM and the finite cell method, Comput. Mech. 63 (2019) 1283–1300, https://doi.org/10.1007/s00466-018-1649-7.
[35] R.U. Patil, B.K. Mishra, I.V. Singh, An adaptive multiscale phase field method for brittle fracture, Comput. Methods Appl. Mech. Eng. 329 (2018) 254–288, https://doi.org/10.1016/j.cma.2017.09.021.

[36] G. Molnár, A. Gravouil, 2D and 3D Abaqus implementation of a robust staggered phase-field solution for modeling brittle fracture, Finite Elem. Anal. Des. 130 (2017) 27–38, https://doi.org/10.1016/j.finel.2017.03.002.
[37] H. Amor, J.J. Marigo, C. Maurini, Regularized formulation of the variational brittle fracture with unilateral contact: numerical experiments, J. Mech. Phys. Solids 57 (2009) 1209–1229, https://doi.org/10.1016/j.jmps.2009.04.011.
[38] J.Y. Wu, V.P. Nguyen, A length scale insensitive phase-field damage model for brittle fracture, J. Mech. Phys. Solids 119 (2018) 20–42, https://doi.org/10.1016/j.jmps.2018.06.006.
[39] J.Y. Wu, Y. Huang, Comprehensive implementations of phase-field damage models in Abaqus, Theor. Appl. Fract. Mech. 106 (2020) 102440, https://doi.org/10.1016/j.tafmec.2019.102440.
[40] M. Seiler, T. Linse, P. Hantschke, M. Kästner, An efficient phase-field model for fatigue fracture in ductile materials, Eng. Fract. Mech. 224 (2020) 106807, https://doi.org/10.1016/j.engfracmech.2019.106807.
[41] C. Miehe, F. Aldakheel, A. Raina, Phase field modeling of ductile fracture at finite strains: a variational gradient-extended plasticity-damage theory, Int. J. Plast. 84 (2016) 1–32, https://doi.org/10.1016/j.ijplas.2016.04.011.
[42] C. Miehe, D. Kienle, F. Aldakheel, S. Teichtmeister, Phase field modeling of fracture in porous plasticity: a variational gradient-extended Eulerian framework for the macroscopic analysis of ductile failure, Comput. Methods Appl. Mech. Eng. 312 (2016) 3–50, https://doi.org/10.1016/j.cma.2016.09.028.
[43] C. Huang, X. Gao, Development of a phase field method for modeling brittle and ductile fracture, Comput. Mater. Sci. 169 (2019) 109089, https://doi.org/10.1016/j.commatsci.2019.109089.
[44] H. Jafarzadeh, G.H. Farrahi, V.I. Levitas, M. Javanbakht, Phase field theory for fracture at large strains including surface stresses, Int. J. Eng. Sci. 178 (2022) 103732, https://doi.org/10.1016/j.ijengsci.2022.103732.
[45] M. Ambati, T. Gerasimov, L. De Lorenzis, Phase-field modeling of ductile fracture, Comput. Mech. 55 (2015) 1017–1040, https://doi.org/10.1007/s00466-015-1151-4.
[46] M.J. Borden, T.J.R. Hughes, C.M. Landis, A. Anvari, I.J. Lee, A phase-field formulation for fracture in ductile materials: Finite deformation balance law derivation, plastic degradation, and stress triaxiality effects, Comput. Methods Appl. Mech. Eng. 312 (2016) 130–166, https://doi.org/10.1016/j.cma.2016.09.005.
[47] R. Alessi, M. Ambati, T. Gerasimov, S. Vidoli, L. De Lorenzis, Comparison of phase-field models of fracture coupled with plasticity, E. Oñate, D. Peric, E. de Souza Neto, M. Chiumenti (Eds.). Advances in Computational Plasticity: a Book in Honour of D. Roger J. Owen, Springer International Publishing, Cham, 2018, pp. 1–21, https://doi.org/10.1007/978-3-319-60885-3_1.
[48] G. Molnár, A. Gravouil, R. Seghir, J. Réthoré, An open-source Abaqus implementation of the phase-field method to study the effect of plasticity on the instantaneous fracture toughness in dynamic crack propagation, Comput. Methods Appl. Mech. Eng. 365 (2020) 113004, https://doi.org/10.1016/j.cma.2020.113004.
[49] D. Moens, D. Vandepitte, Recent advances in non-probabilistic approaches for non-deterministic dynamic finite element analysis, Arch. Comput. Methods Eng. 13 (2006) 389–464, https://doi.org/10.1007/BF02736398.
[50] V.H. Truong, S. Tangaramvong, G. Papazafeiropoulos, An efficient LightGBM-based differential evolution method for nonlinear inelastic truss optimization, Expert Syst. Appl. 237 (2024) 121530, https://doi.org/10.1016/j.eswa.2023.121530.
[51] P. Nuaklong, K. Hamcumpai, S. Keawsawasvong, S. Pethrung, P. Jongvivatsakul, S. Tangaramvong, T. Pothisiri, S. Likitlersuang, Strength and post-fire performance of fiber-reinforced alkali-activated fly ash concrete containing granite industry waste, Constr. Build. Mater. 392 (2023) 131984, https://doi.org/10.1016/j.conbuildmat.2023.131984.
[52] V.H. Truong, H.A. Pham, T. Huynh Van, S. Tangaramvong, Evaluation of machine learning models for load-carrying capacity assessment of semi-rigid steel structures, Eng. Struct. 273 (2022) 115001, https://doi.org/10.1016/j.engstruct.2022.115001.
[53] Y. Yu, B. Dong, W. Gao, A. Sofi, Physics-based stochastic aging corrosion analysis assisted by machine learning, Probabilistic Eng. Mech. 69 (2022) 103270, https://doi.org/10.1016/j.probengmech.2022.103270.
[54] Y. Liu, Y. Feng, D. Wu, X. Chen, W. Gao, Virtual modelling integrated phase field method for dynamic fracture analysis, Int. J. Mech. Sci. 252 (2023) 108372, https://doi.org/10.1016/j.ijmecsci.2023.108372.
[55] A.A. Griffith, The phenomena of rupture and flow in solids, Philos. Trans. R. Soc. Lond. Ser. A, 221 (1921) 163–198. Containing Papers of a Mathematical or Physical Character.
[56] F. Freddi, G. Royer-Carfagni, Regularized variational theories of fracture: a unified approach, J. Mech. Phys. Solids 58 (2010) 1154–1174, https://doi.org/10.1016/j.jmps.2010.02.010.
[57] C. Miehe, M. Hofacker, F. Welschinger, A phase field model for rate-independent crack propagation: Robust algorithmic implementation based on operator splits, Comput. Methods Appl. Mech. Eng. 199 (2010) 2765–2778, https://doi.org/10.1016/j.cma.2010.04.011.
[58] R. Rebba, S. Mahadevan, Computational methods for model reliability assessment, Reliab. Eng. Syst. Saf. 93 (2008) 1197–1207, https://doi.org/10.1016/j.ress.2007.08.001.
[59] B. Goller, H.J. Pradlwarter, G.I. Schuëller, Reliability assessment in structural dynamics, J. Sound Vib. 332 (2013) 2488–2499, https://doi.org/10.1016/j.jsv.2012.11.021.
[60] R. Fletcher, Practical Methods of Optimization, John Wiley & Sons, 2000.
[61] J.H. Argyris, L.E. Vaz, K.J. Willam, Integrated finite-element analysis of coupled thermoviscoplastic problems, J. Therm. Stress. 4 (1981) 121–153, https://doi.org/10.1080/01495738108909960.
[62] C.N. Wong, J. Xiong, H.Z. Huang, T. Hu, Damage detection of space truss using second order polynomial method with BFGS Quasi-Newton optimization, in: Proceedings of the ASME 2010 International Design Engineering Technical Conferences and Computers and Information in Engineering Conference, 2010, pp. 753–762, https://doi.org/10.1115/detc2010-28091.
[63] J.Y. Wu, Y. Huang, V.P. Nguyen, On the BFGS monolithic algorithm for the unified phase field damage theory, Comput. Methods Appl. Mech. Eng. 360 (2020) 112704, https://doi.org/10.1016/j.cma.2019.112704.
[64] H. Drucker, C.J. Burges, L. Kaufman, A. Smola, V. Vapnik, Support vector regression machines, Adv. Neural Inf. Process. Syst. 9 (1996) 155–161.
[65] L. Wang, J. Zhu, H. Zou, The doubly regularized support vector machine, Stat. Sin. 16 (2006) 589–615.
[66] J. Li, K. Cheng, S. Wang, F. Morstatter, R.P. Trevino, J. Tang, H. Liu, Feature selection: a data perspective, ACM Comput. Surv. 50 (2017) 94, https://doi.org/10.1145/3136625. Article.
[67] Y. Feng, Q. Wang, Y. Yu, T. Zhang, D. Wu, X. Chen, Z. Luo, W. Gao, Experimental-numerical-virtual (ENV) modelling technique for composite structure against low velocity impacts, Eng. Struct. 278 (2023) 115488, https://doi.org/10.1016/j.engstruct.2022.115488.
[68] D. Madani, Park Shuts Down Roller Coaster After Visitor Spots Cracked Support Beam Shift Out of Place as Coaster Speeds Past, NBC News, 2023.
[69] J.A. Raynal Villaseñor, Normal distribution, J.A. Raynal Villaseñor (Ed.). Frequency Analyses of Natural Extreme Events: a Spreadsheets Approach, Springer International Publishing, Cham, 2021, pp. 39–59, https://doi.org/10.1007/978-3-030-86390-6_3.
[70] S.D. Moitra, Skewness and the Beta Distribution, J. Oper. Res. Soc. 41 (1990) 953–961, https://doi.org/10.2307/2583273.
[71] G. Arslan, M. Ahsanullah, I.G. Bayramoglu, On characteristic properties of the uniform distribution, Sankhyā Indian J. Stat. 2003-2007 67 (2005) 715–721.
[72] J.H. Chen, S.H. Cho, An accessory technique for the intraoral removal of a fractured implant abutment screw, J. Prosthet. Dent. 120 (2018) 812–815, https://doi.org/10.1016/j.prosdent.2018.01.026.